

# Local current analysis on defective zigzag graphene nanoribbons devices for biosensor material applications

Jingjing Shao<sup>1</sup> | Beate Paulus<sup>1</sup> | Jean Christophe Tremblay<sup>2</sup>

<sup>1</sup>Institut für Chemie und Biochemie, Freie Universität Berlin, Berlin, Germany

<sup>2</sup>Laboratoire de Physique et Chimie Théoriques, CNRS-Université de Lorraine, UMR 7019, ICPM, Metz

## Correspondence

Jingjing Shao, Institut für Chemie und Biochemie, Freie Universität Berlin, Arnimallee 22, 14195 Berlin, Germany.  
 Email: jingjingshao@zedat.fu-berlin.de

Jean Christophe Tremblay, Laboratoire de Physique et Chimie Théoriques, CNRS-Université de Lorraine, UMR 7019, ICPM, 1 Bd Arago, 57070 Metz, France.  
 Email: jean-christophe.tremblay@univ-lorraine.fr

## Abstract

In this contribution, we aim at investigating the mechanism of biosensing in graphene-based materials from first principles. Inspired by recent experiments, we construct an atomistic model composed of a pyrene molecule serving as a linker fragment, which is used in experiment to attach certain aptamers, and a defective zigzag graphene nanoribbons (ZGNRs). Density functional theory including dispersive interaction is employed to study the energetics of the linker absorption on the defective ZGNRs. Combining non-equilibrium Green's function and the Landauer formalism, the total current-bias voltage dependence through the device is evaluated. Modifying the distance between the linker molecule and the nanojunction plane reveals a quantitative change in the total current-bias voltage dependence, which correlates to the experimental measurements. In order to illuminate the geometric origin of these variation observed in the considered systems, the local currents through the device are investigated using the method originally introduced by Evers and co-workers. In our new implementation, the numerical efficiency is improved by applying sparse matrix storage and spectral filtering techniques, without compromising the resolution of the local currents. Local current density maps qualitatively demonstrate the local variation of the interference between the linker molecule and the nanojunction plane.

## 1 | INTRODUCTION

The successful isolation of the graphene in 2004<sup>1–4</sup> has opened new avenues for designing new generation of transistor materials.<sup>5–7</sup> The chemical nature of its  $\pi$  system leads an ultrahigh electron mobility, which is one determining feature for potential utility in electronics. Yet, the absence of band gap in graphene does not result in a controllable on/off ratio, which is critical and essential for the utilization as transistors. Different approaches have been investigated in order to modify graphene's electronic properties and further improve its on/off ratio upon application of a bias voltage. The creation of graphene nanostructures with lateral quantum confinement (e.g., graphene dots and nanoribbons) has been broadly explored to introduce a finite band

gap. Graphene nanomeshes, continuous 2D graphene nanostructures with a high density of vacancies, have been created for this endeavor. As a specific example, graphene antidots lattices (GALs), created by a regular hexagonal perforation of a graphene sheet, is another effective approach to modify the electronic properties of graphene, which have been studied extensively both at experimental<sup>8–11</sup> and theoretical levels.<sup>12–16</sup> A recent publication<sup>11</sup> reported the successful synthesis of such material. Apart from their exceptional mechanical strength and flexibility, these materials are suggested to hold great promises for the application as biosensors. By incorporating functional groups with specific chemical or biological recognition ability, defective GALs can be used to detect various bio molecules, exploiting their tunable on/off ratio when a bias voltage is applied. In the reported application, the

This is an open access article under the terms of the Creative Commons Attribution-NonCommercial-NoDerivs License, which permits use and distribution in any medium, provided the original work is properly cited, the use is non-commercial and no modifications or adaptations are made.

© 2021 The Authors. *Journal of Computational Chemistry* published by Wiley Periodicals LLC.

HER2 protein is subject to a selective interaction with aptamers attached to a linker fragment deposited on the GAL surface, which in turn induced a change in the electrical signal. The significant increase in the drain current (120 nA) after attachment to the aptamers thereby allowed label-free detection of HER2 proteins. With the higher concentration of the proteins, higher conductance is measured. It was also observed that GALs exhibit a higher protein binding amount than that of graphene, possibly due to the increased edge sites around the pores and enlarged surface area. Additionally, the rich edge sites around the defects may also facilitate the functionalization of specific receptors for the creation of highly specific biosensors. These active-sites are potentially affected by an external perturbation, such as the presence of a linker binding selectively to a protein.<sup>17,18</sup>

Despite these experimental successes, the mechanism of bio detection in such devices remains unclear. A potentially powerful tool in this endeavor is the investigation of the transport properties combining local current analysis of the device within non-equilibrium Green's function (NEGF) framework.<sup>19–28</sup> This yields complementary information about the total amount of current as a function of the applied bias voltage and the mechanism of charge transport through the device. In previous work,<sup>29</sup> similar structures based on pristine and defective zigzag graphene nanoribbons (ZGNR) have been investigated, where detailed information about local current properties have been analyzed. It was found, that the current preferentially flows laminarly along the defect edges, and that it follows a meandering path between those defects. In this present work, we aim at understanding the mechanism of biosensing in graphene-based materials by applying this technique. We intend to investigate the variations of the current in defective ZGNRs upon the influence of a pyrene molecule, which serves as a linker fragment. Scanning favorable absorption site of the linker molecule around defect reveals the influence of the perforations of chosen nanosheets in comparison to pristine graphene sheet. By varying the distance between the linker fragment and ZGNRs sheet, the effect of the presence of the HER2 protein is simulated. The system is represented by a model Hamiltonian describing the nanojunction, parameterized from first principles using density functional theory (DFT) following a procedure described in References 23, 27, 29–31. This first yields information about favorable adsorption site of the linker on the defective ZGNRs and the nature of their interaction. The current variations under different conformations is revealed with NEGF formalism and Lander equation. The local currents are computed in a real grid representation using a procedure introduced by Evers and co-workers.<sup>19–21</sup> To reduce the computational demand associated with the large nanostructures used in this work, we introduce two modifications to the previous scheme: a reduction of the atomic orbitals basis and the derivatives in grid representations using sparse matrix storage, and spectral filtering of the Green's function via reduced singular value decomposition. This combination of techniques amounts to significant numerical savings and leads to an efficient procedure to study the local current maps in the linker-ZGNRs system.

The paper is organized as follows: in Section 2, we summarize the procedure to parametrize and construct the device Hamiltonian, together with the description of the theory for computing the local currents. Section 3 reports on the main findings of this work, from the energetics of the adsorption to the total and local current information.

Section 4 presents a critical discussion of the results, which is followed by a general conclusion in Section 5.

## 2 | THEORY

### 2.1 | Model construction

To study the transport properties of the linker-defective ZGNRs system, we use a model system composed of a finite scattering region connected with two semi-infinite leads as shown in Figure 1. It is noted that the underlying difference between the model and the experimental setup is their dimensional scales. A 2D GAL embedded between two graphene electrodes is used in the biosensing experiment, whereas 1D nanojunction model is used here. In our previous work,<sup>29</sup> we have shown that the mechanistic information about electron transport can be well studied from the local current properties in those 1D nanojunctions models. We therefore postulate that the proposed 1D linker-defective ZGNR system is sufficient to understand the experimentally measurable trends qualitatively. Following the conventional notation, a ZGNR is characterized by the number of zig-zag chains along the ribbon forming its width. Here, we have used 6ZGNR to mimic the finite width of a graphene sheet. The defects are formed with hexagonal carbon vacancies, and all dangling  $\sigma$  bonds around the defect edge are saturated with hydrogen atoms. Throughout this work, all systems of interest include two defects that are separated by two slice units, where one unit is defined as two carbon atoms width along the ribbon. It is noted that (quasi-) 1D structure are used as an approximation to the experimental nanosheet and the width of the ZGNRs are chosen in a such way that no disturbance in the local current density near the edge of the ZGNRs is observed, due to the presence of the linker molecule. The spin restricted solutions are chosen so that no edge effects of the ZGNRs are taken into considerations. This is compatible with the experimental setup, where a 2D graphene nanomesh with a high density of perforations is used and for which spin polarization and edge effects play a negligible role.

The parameterized Hamiltonian of the complete system is specified by three Hamiltonian matrix blocks,  $H_{\text{scat}}$ ,  $H_L$  and  $H_R$ , for the three specified regions. The blocks are constructed by partitioning the total Hamiltonian of the molecular structure in the basis of atomic orbitals using Mulliken projectors, so that the influence of the complete system on different regions is taken into account.<sup>31,32</sup> The nanojunction of interest (pink region in Figure 1) includes two defects separated by two slice units. A buffer region composed of ZGNRs units surrounds the defective ZGNRs scattering region. The buffer units serve to reduce the numerical errors at the edges of the leads and of the scattering region<sup>29,31</sup> and the convergence of size of the buffer units are already presented in our previous publication.<sup>29</sup> The leads (purple boxes in Figure 1) are connected on either sides of the buffer region. A supplementary ZGNR slice unit saturated with hydrogen atoms is used to close the molecular model on each side of the cluster, and they are neglected in the parametrization of the system Hamiltonian.

The coupling between the lead units and the scattering region is described by the off-diagonal blocks of the parametrized Hamiltonian. The lead diagonal block of the Hamiltonian gives information about the

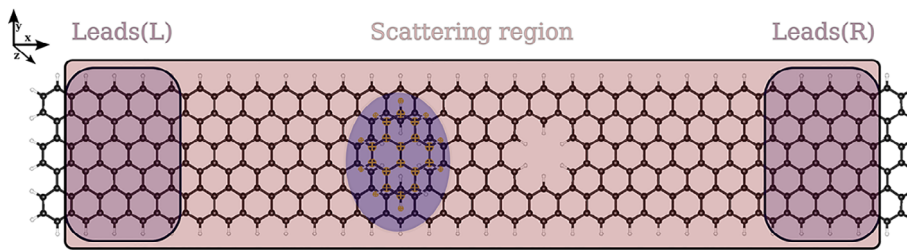


**FIGURE 1** Representation of a transport model with two defects and a pyrene molecule placed on top of the leftmost defect. The carbon atoms of the zigzag graphene nanoribbon (ZGNR) nanojunction are drawn in black and hydrogen atoms in white. A pyrene linker adsorbed on the ZGNR is marked in yellow. The nanojunction is partitioned into three parts: The central scattering region (pink) and two lead parts (L/R, in purple). The outer hydrogen atoms and first slices of edge carbon atoms, which are not included in the color boxes, are neglected in the construction of the complete system Hamiltonian. The leads part of the transport Hamiltonians shown in the purple boxes are repeated to mimic semi-infinite leads

on-site energies of the leads. To simulate semi-infinite leads, the lead diagonal block of the Hamiltonian is replaced by the diagonal block of a dimer model of the leads, in which the scattering and buffer regions have been omitted. The off-diagonal blocks of the dimer model describing the coupling between two lead units are used to extend the leads. This extension procedure<sup>23,27,31</sup> is repeated until convergence of the total current through the nanojunction is obtained. In Figure 1, a linker molecule (marked in yellow) similar to the one shown in Yang et al.<sup>11</sup> is chosen: a pyrene molecule, which is composed of four fused benzene rings. This linker molecule is placed on different adsorption sites around the defect position in the following simulations.

## 2.2 | Transport calculations

The total current flowing through the device is calculated using the NEGF formalism. This first requires the determination of the transmission function, which is calculated using the following expression

$$T(E) = \text{Tr}[G'(E)\Gamma_L(E)G^a(E)\Gamma_R(E)] \quad (1)$$

where the Green's function is given as

$$G'^a(z) = (zS_{\text{scat}} - H_{\text{scat}} - \Sigma_L(z) - \Sigma_R(z))^{-1} \quad (2)$$

Here,  $H_{\text{scat}}$  and  $S_{\text{scat}}$  are Hamiltonian and overlap matrices of the scattering region, and  $z = E \pm i0^+$  define respectively the retarded and advanced Green's function,  $G'^a(z)$ . The self-energies  $\Sigma_{L/R}(z)$  describe the effect of the semi-infinite leads L and R on the scattering region. From the transmission function, the zero-voltage conductance is obtained from the expression  $\frac{2e^2}{h}T(E_F)$ , where  $e$ ,  $h$  and  $E_F$  are respectively the elementary charge, Planck's constant, and the Fermi energy of the system. The spectral broadening matrices in the transmission function are given by  $\Gamma_{L/R} = i(\Sigma_{L/R} - \Sigma_{L/R}^a)$ , which account for the level broadening in the scattering region due to the coupling to the leads. When a bias voltage is applied between the leads,  $(-e)V_{\text{voltage}} = \mu_R - \mu_L$ , the total current is given by

$$I_e = 2\frac{-e}{h} \int_{-\infty}^{+\infty} T(E)(f_L(E) - f_R(E))dE \quad (3)$$

where the  $f_{L/R}(E)$  are the Fermi distribution functions of the left and right contacts, and the factor 2 accounts for the degenerate spin channels.

## 2.3 | Local current density

For the current density calculation, we follow the approach developed in References 19–21. The non-equilibrium Keldysh Green's function  $G^<(E)$  (lesser Green's function) is calculated from the advanced and retarded Green's function as

$$G^<(E) = iG'(E)[f_L(E)\Gamma_L + f_R(E)\Gamma_R]G^a(E) \quad (4)$$

In order to obtain a real-space representation of the local current, the lesser Green's function can be expanded using the atomic orbitals basis ( $\psi_{\mu_A/\nu_B}(\mathbf{r})$ ) at position  $\mathbf{r}$  as

$$G^<(\mathbf{r}, \mathbf{r}', E) = \sum_{A,B} \sum_{\mu_A \nu_B} \psi_{\mu_A}(\mathbf{r}) G^<_{\mu_A \nu_B}(E) \psi_{\nu_B}(\mathbf{r}') \quad (5)$$

The local current density can be then represented as a spatial derivative of the Keldysh function

$$j(\mathbf{r}, E) = \frac{1}{2\pi m} \sum_{A,B} \sum_{\mu_A \nu_B} \psi_{\mu_A}(\mathbf{r}) G^{as} \nabla \psi_{\nu_B}(\mathbf{r}) \quad (6)$$

where  $G^{as}$  stands for the antisymmetric elements of the lesser Green's function,  $\frac{1}{2}(G^<_{\mu_A \nu_B} - G^<_{\nu_B \mu_A})$ . As all the matrix elements in Equation (6) are in real grid space representation and selected grids in such large nanostructures are dense, high computational demand on matrix elements storage and the evaluation process of the current density is required.

In order to improve the computational efficiency, two numerical techniques are introduced to evaluate Equation (6): a real space filter using the compressed row storage (CRS) format,<sup>33</sup> and a spectral filter based on single value decomposition (SVD). In the standard CRS format, only elements different from zero are stored in three arrays, which respectively contain the values and the associated row and column indices. Here, we apply the CRS on the atomic orbitals basis  $\psi_{\mu_A}(\mathbf{r})$  matrix and the derivatives thereof, in a such way that only values larger than the chosen threshold are stored. Since the atomic orbitals and their derivatives are strongly localized around atoms, their real-space contribution vanishes rapidly for atoms that are far apart in the nanostructure. For the present application, the  $N_{\text{atoms}} = 312$  atoms of the scattering and buffer regions are represented using  $N_{\text{ao}} = 3560$  atomic orbitals projected on a real-space Cartesian grid of dimension  $\{N_x = 151, N_y = 32, N_z = 14\}$  (total grid size  $N_{\text{grid}} = 67'648$ ). Choosing a threshold of 1% of the maximum value amounts to a reduction of the atomic orbital basis matrix from  $N_{\text{atoms}} \times N_{\text{grid}} = 240'826'880 - 939'638$  elements, and similar savings for the derivative matrices (766'205, 762'162, and 797'111 for the derivative w.r.t.  $\{x, y, z\}$ ). This reduces the disc usage from 7.7 to 0.01 Gbyte.

A spectral filter using the SVD technique is then applied to the matrix  $\mathbf{G}^{\text{as}}$  containing the antisymmetric elements of the lesser Green's function, which takes the form:

$$\mathbf{G}^{\text{as}} = \mathbf{U}\Sigma\mathbf{V}^T \quad (7)$$

where  $\Sigma = \text{diag}(\sigma_1, \sigma_2, \dots)$  is the diagonal matrix of singular values, and  $\{\mathbf{U}, \mathbf{V}\}$  are matrices containing the associated singular vectors. By selecting only the  $N_{\text{red}}$  prominent values of  $\Sigma$ , one can potentially reduce all computational operation steps without substandard resolution. The underlying assumption is that the spectral information of  $\mathbf{G}^{\text{as}}$  is contained in the reduced number  $N_{\text{red}}$  of important singular vectors. Substituting  $\mathbf{G}^{\text{as}}$  with the reduced diagonal matrix of singular value  $\Sigma_{\text{red}}$  and  $\{\mathbf{U}_{\text{red}}, \mathbf{V}_{\text{red}}\}$  in Equation (6), the local current density takes the form

$$\begin{aligned} j(\mathbf{r}, E) &= \frac{1}{2\pi} \frac{\hbar}{m} \Psi^T(\mathbf{r}) \mathbf{U}_{\text{red}} \Sigma_{\text{red}} \mathbf{V}_{\text{red}}^T \nabla \Psi(\mathbf{r}) \\ &= \frac{1}{2\pi} \frac{\hbar}{m} \Phi^T(\mathbf{r}) \Sigma_{\text{red}} (\nabla \Phi)(\mathbf{r}) \end{aligned} \quad (8)$$

where the matrices  $\Phi(\mathbf{r})$  and  $(\nabla \Phi)(\mathbf{r})$  are obtained by linear transformations using the rectangular matrices of the singular vectors, that is,

$$\Phi(\mathbf{r}) = \mathbf{U}_{\text{red}}^T \Psi(\mathbf{r}); (\nabla \Phi)(\mathbf{r}) = \mathbf{V}_{\text{red}}^T \nabla \Psi(\mathbf{r}) \quad (9)$$

Matrix  $\mathbf{G}^{\text{as}}$  has originally a size of  $N_{\text{ao}} \times N_{\text{ao}}$ . By taking only the largest  $N_{\text{red}}$  values, matrix  $\mathbf{U}_{\text{red}}$  has the size of  $N_{\text{ao}} \times N_{\text{red}}$ ,  $\Sigma_{\text{red}}$  is a diagonal matrix with the size of  $N_{\text{red}} \times N_{\text{red}}$ , and matrix  $\mathbf{V}_{\text{red}}^T$  has size of  $N_{\text{red}} \times N_{\text{ao}}$ . In total, the  $N_{\text{ao}}$  multiplication steps in Equation (6) are reduced to  $N_{\text{red}}$  steps in Equation (8). For the specific system below, where  $N_{\text{ao}} = 3560$  and  $N_{\text{red}} = 50$ , this represents two orders of magnitude in computational savings. A benchmark calculation without

CRS and SVD filtering is shown in the Figure S1 for resolution assessment.

The total local current is obtained by integration of the local current density over the energy window, which is defined by the applied bias voltage

$$J(\mathbf{r}) = 2 \int j(\mathbf{r}, E) dE \quad (10)$$

where the factor 2 accounts for degenerate spin channels in the case of spin-restricted systems.

## 2.4 | Computational set-up

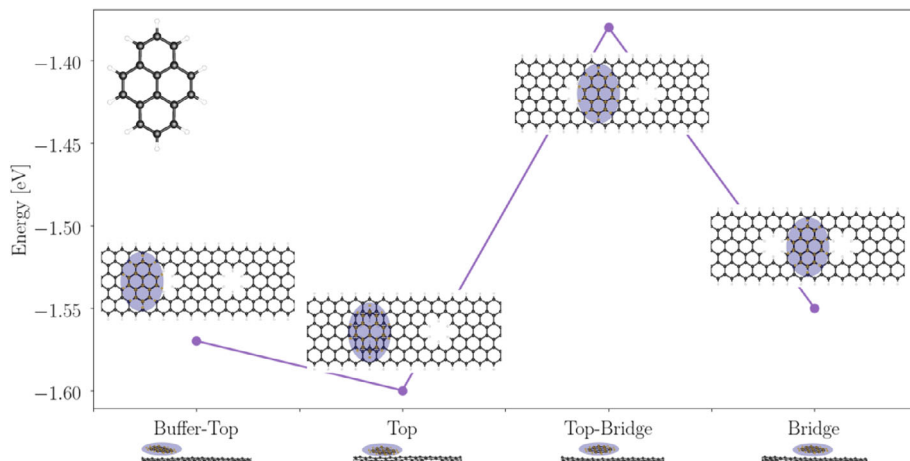
To determine the parameters to be used for the Hamiltonian matrices elements in Figure 1, DFT calculations are performed using the GPAW<sup>34,35</sup> package. The structure optimization of the whole linker-nanojunction systems employ the libxc<sup>36,37</sup> implementation of the opt-PBE-vdW functional,<sup>38,39</sup> which provides an efficient treatment of the non-local van der Waals (vdW) interaction in the considered systems. The wave functions are represented using a numerical double  $\zeta$  polarized (dzp) basis set.<sup>40</sup> During the structure optimization, atomic positions are varied until the remaining forces are less than 0.02 eV/Å. The density matrix is integrated using a Fermi-Dirac distribution with  $k_B T$  value of 0.01 eV, which is essential to obtain converged DFT results. The wave functions are represented with a grid spacing of 0.18 Å. The electronic transport calculations are done via the atomic simulation environment implementation of the NEGF formalism.<sup>41-45</sup> All atomic orbitals and their derivatives are projected on a grid using ORBKIT.<sup>46-48</sup> For the semi-infinite leads the computational cell is sampled using 20 Monkhorst-Pack K-points along the periodic direction.

## 3 | RESULTS

### 3.1 | Energetics at different adsorption sites

In order to find the preferable site for the linker absorption on the nanojunction surface, we perform an energetic analysis of the pyrene molecule placed at four special points along x-axis around the first defect. Due to the mirror symmetry of selected nanojunction, the first and the second defect share same geometric character. Therefore, positions around the leftmost defect are sufficient to represent the rightmost one. The orientation of the pyrene molecule in reference to the nanojunction is selected as shown in Figure 2, where the center of the linker molecule and the defect are aligned with each other. Test calculations for the linker molecule rotation at the Bridge position reveals marginal energy difference among different conformations. It shows a small energetic barrier with highest value of 0.03 eV (Figure S2). This indicates that the linker molecule can undergo a relatively free rotation parallel to the nanojunction plane.

**FIGURE 2** Absorption energies of the system with linker molecule placed at four different special positions: Buffer-top, top, top-bridge and bridge. On top of the defect is noted as top position and pristine zigzag graphene nanoribbons (ZGNRs) region between the defects is noted as bridge position. The carbon atoms and the hydrogen atoms in the nanosheet are drawn in black and white, respectively. The linker molecule is marked in yellow. Both top and side views of the finite scattering region of the absorption systems are illustrated. The top view of the pyrene molecule is illustrated in the upper left



During this set of structural optimizations, the z-axis of both nanojunction and the linker molecule are not constrained, which allows to find the most stable equilibrium distance in each case.

The absorption energies shown in Figure 2 are determined by subtracting the total energies of the absorption system from the sum over free standing nanojunction and the pyrene molecules (all results reported in eV). The site at the interface between the buffer region and the leftmost defect (Buffer-Top) is found at an adsorption energy of  $-1.58$  eV. Adsorption on top of the defect (Top) is found to have the lowest absorption energy, with the value of  $-1.60$  eV. When the linker molecule is placed at the right and edge of the leftmost defect (Top-Bridge), the absorption energy rises up to  $-1.38$  eV, whereas the energy lowers to  $-1.55$  eV when the linker is on top of the pristine ZGNRs region between the two defects (Bridge). From these values, the Top position appears as the energetically more favorable absorption site among the examined points. The Bridge position is a local minimum, which is connected to the Top position by a  $0.25$  eV translational energy barrier (see the Top-Bridge position). Consequently, only these two structures at local minima are chosen to perform further investigations, where the distance between the linker and the nanojunction is varied.

### 3.2 | Effect of linker-defective ZGNRs distance on device energetics and structure

In what follows, we investigate different conformations of the systems, which are formed through varying the distance between the linker fragment and the defective ZGNR surface. In the experiment, the total conductance of those biosensor materials is measured upon the attachment of a protein to the linker. This protein binding will lead to a change in height of the linker with respect to the ZGNR basal plane. To mimic the experimental situation where the finite central part is connected to two fixed electrodes, the linker is manually brought closer to nanojunction plane along the z-axis. In this set of structural optimizations, the leads part in the nanojunction are fully constrained and the initial z-axis position of the linker molecule in

reference to the nanojunction plane is constrained. Under these conditions, only the scattering region of the nanojunction has full freedom of motion during the optimization.

At the Top position, five different initial distances including the equilibrium ( $Z_{eq}$ ) are investigated. In Figure 3, the absorption energies (in eV) of each considered systems are shown, together with their structure in side view. The equilibrium distance between the linker fragment at the Top position and defective ZGNRs surface is  $Z_{eq} = 3.2$  Å, which confirms the expected dispersive character to the interaction. When the linker absorption on defective ZGNRs is fixed at  $1.0$  or  $0.5$  Å above  $Z_{eq}$ , the defective ZGNR surface plane remains flat and no geometrical influence of the linker molecule on the nanojunction is observed. The absorption energy, however, decreases by more than  $0.4$  eV from  $Z_{eq} + 1.0$  to  $Z_{eq} + 0.5$  position. At  $Z_{eq}$ , the defective ZGNR surface remains flat and the linker absorption energy is found to be lowest. When moving the linker molecule  $0.5$  Å closer to the nanojunction, the defective ZGNR surface becomes distorted. In particular, the carbon atoms around the defects move away from the linker and induce a large buckling in the nanojunction, as illustrated in the left panel in Figure 3. The absorption energy increases slightly in comparison to the  $Z_{eq}$  position. This destabilizing effect is enhanced when the linker molecule is moved increasingly closer (see  $Z_{eq} - 1.0$ ). The carbon atoms around the defect in the nanojunction sheet move further away from their original equilibrium z-axis positions. The largest change is found at edge hydrogen and carbon atoms of the defect. They are  $\sim 1.0$  Å lower than their original z-positions. In the two lowest adsorption positions, the distance between the linker molecule and the defect edge carbon atoms remain  $3.2$  Å. From the energetic perspective, the linker remains relatively stable, with an absorption energy of  $-1.4$  eV for the lowest position at  $Z_{eq} - 1.0$ , which represents only an increase of  $0.2$  eV relative to the  $Z_{eq}$  position.

A similar energetic scan is performed for the systems with the linker molecule at the Bridge position. Five different initial distances between the linker molecule with respect to the nanojunction plane are selected. In this particular case, as the linker has a stronger geometric influence on the defective ZGNRs surface at larger distances,

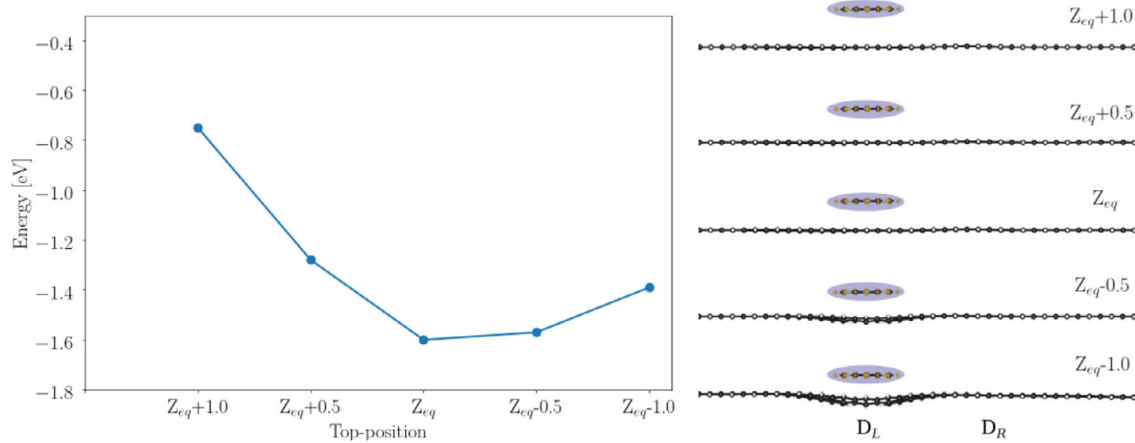


**FIGURE 3** Absorption energies of the system with linker molecule placed at the top position with five different initial distances relative to the nanojunction:  $Z_{eq} + 1.0$ ,  $Z_{eq} + 0.5$ ,  $Z_{eq}$ ,  $Z_{eq} - 0.5$  and  $Z_{eq} - 1.0$ . The notation refers to the initial distance between the linker molecule and the nanojunction before structure optimization. The side views of the relaxed scattering region are illustrated in the right panels

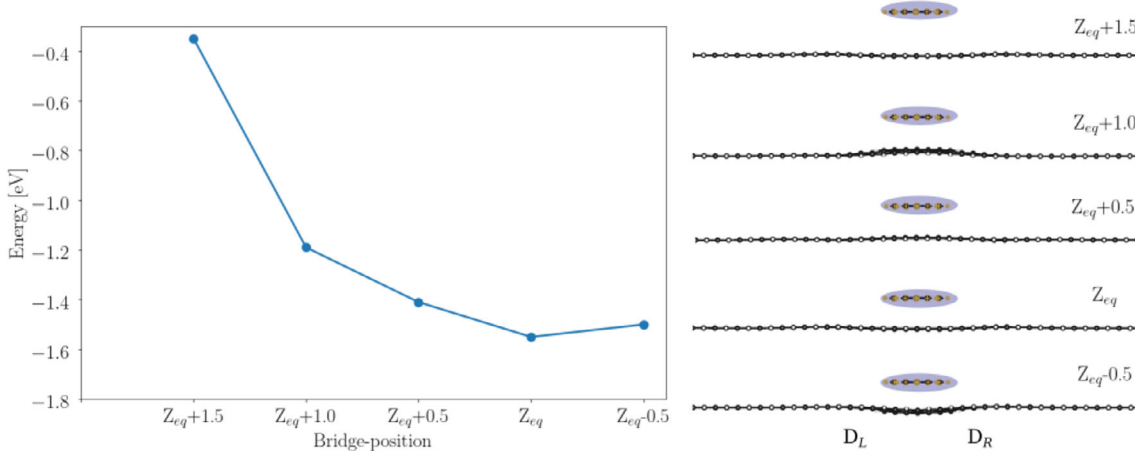


**FIGURE 4** Absorption energies of the system with linker molecule placed at the bridge position with five different initial distances relative to the nanojunction:  $Z_{eq} + 1.5$ ,  $Z_{eq} + 1.0$ ,  $Z_{eq} + 0.5$ ,  $Z_{eq}$  and  $Z_{eq} - 0.5$ . The notation refers to the initial distance between the linker molecule and the nanojunction before structure optimization. The side views of the relaxed scattering region are illustrated in the right panels

the highest position is set to  $Z_{eq} + 1.5$  instead of  $Z_{eq} - 0.5$ . At the Bridge position, the equilibrium distance between the linker molecule and the defective ZGNRs surface is found at  $Z_{eq} = 3.4 \text{ \AA}$ . This value again suggests a dispersive interaction between the two fragments, and it is 0.2 \AA larger than the one obtained in the  $Z_{eq}$  system with the linker molecule placed at the Top position. Let us start with the furthest distance at  $Z_{eq} + 1.5$ . The defective ZGNRs surface shows no significant buckling in the presence of the linker molecule, and the carbon atoms below the linker are only slightly pushed downwards. A relatively weak adsorption energy at  $-0.38 \text{ eV}$  is found. When the linker molecule is moved closer to the nanojunction surface (see  $Z_{eq} + 1.0$ ), the carbon atoms from the defective ZGNRs surface, which are just beneath the linker molecule, moves out of the planar nanojunction plane and toward the linker. This effect results in a strong geometric distortion. The distance between the linker molecule and the defective ZGNRs now reaches the same value as in the equilibrium, 3.4 \AA. A similar effect, albeit with much less intensity,

is observed at the  $Z_{eq} + 0.5$  position. Over a span of 1 \AA, the system is stabilized by  $\sim 0.2 \text{ eV}$  from  $Z_{eq} + 1.0$  to  $Z_{eq} + 0.5$ , and by another 0.2 eV from  $Z_{eq} + 0.5$  to the equilibrium position at  $Z_{eq} = 3.4 \text{ \AA}$ . When the linker molecule is placed closer to the nanojunction, the carbon atoms beneath the linker molecule in the defective ZGNRs surface moves away from the linker molecule. This adjustment allows the system to retain its equilibrium distance. The adsorption energy increases slightly relative to the  $Z_{eq}$  system. From an energetic perspective, the absorption energies vary less with each 0.5 \AA step, in comparison to the Top position.

### 3.3 | Total current-bias voltage dependence

Combining the NEGF approach and the Landauer equation (Equation 3), the total current-bias voltage dependence for systems with different conformations are evaluated. The associated

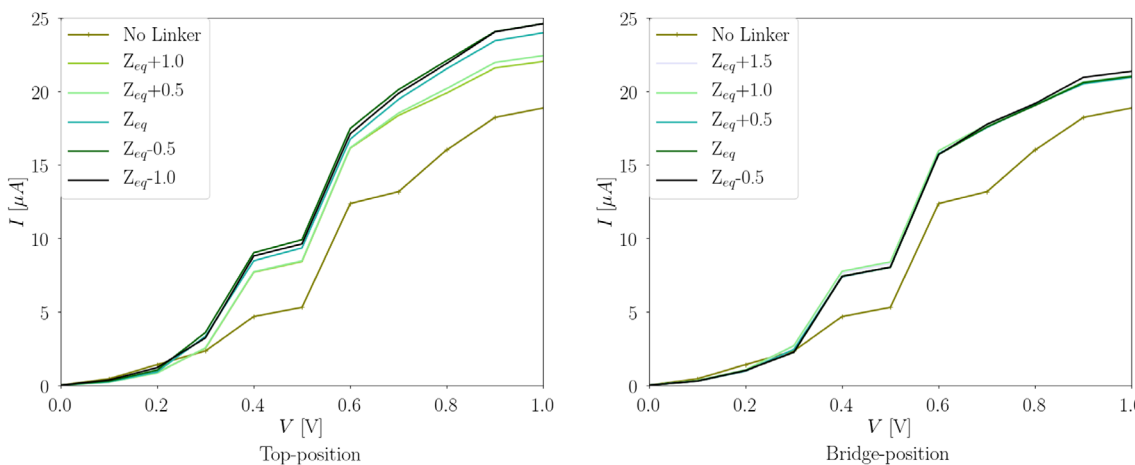


**FIGURE 5** Total current  $I$  ( $\mu\text{A}$ ) in dependence of the applied bias voltage  $V$  (V) with 0.1 V step. The left panel shows the systems with linker placed on the top position, whereas the right panel shows the systems with linker placed on the bridge position. For the top position,  $Z_{\text{eq}} + 1.0$ ,  $Z_{\text{eq}} + 0.5$ ,  $Z_{\text{eq}}$ ,  $Z_{\text{eq}} - 0.5$  and  $Z_{\text{eq}} - 1.0$  systems are considered and for the bridge position,  $Z_{\text{eq}} + 1.5$ ,  $Z_{\text{eq}} + 1.0$ ,  $Z_{\text{eq}} + 0.5$ ,  $Z_{\text{eq}}$  and  $Z_{\text{eq}} - 0.5$  systems are considered. No linker system are included in both figures serving as a reference point

transmission functions can be found in the Figure S3. The chosen structures are illustrated in Figure 3 and in Figure 4, where both absorption positions of the linker and the distance between the linker molecule and the defective ZGNRs are varied. The presence of the linker has a crucial influence on the transport properties of the defective ZGNRs. The IV-curve of the system without linker molecule (No Linker) is plotted in Figure 5 to serve as a reference line. The bias voltage is applied from the left to the right along the  $x$ -axis of the considered systems and all IV-curves are obtained with a 0.1 V step.

All considered conformations in Figure 5 show a gradual increase in the current as a function of applied bias voltage. The slope changes in the IV-curves correspond to new channel opening in the associated transmission functions. Comparing the two adsorption site in Figure 5, the conformation in the left panel have generally a higher conductance than the systems in the right panel. This shows that the Top absorption site of the linker on the nanojunction has a stronger enhancement effect for the conductance in comparison to the Bridge absorption site.

The impact of the linker molecule on the total conductance is not found until the bias voltage reaches 0.3 V. Between 0.3 and 0.5 V, quantitative differences in the conductance start to occur. At the Top position under 0.5 V bias voltage, the  $Z_{\text{eq}}$  system carries almost double the amount of total current than in the system without linker. By shortening the distance between the linker molecule and the defective ZGNRs, a slight increase of the total current is observed under both 0.5 and 1.0 V bias voltages. On the contrary, by increasing the distance between the two, a decrease of the total current in relation to the  $Z_{\text{eq}}$  is favored. Comparing the conformations at  $\pm 0.5 \text{ \AA}$  around  $Z_{\text{eq}}$ , it is notable that an increase in the distance has a stronger impact on the total conductivity than a decrease in the linker-to-surface distance. Comparison between the conformation at  $Z_{\text{eq}} + 1.0$  and the system without linker emphasizes the impact of the presence of the linker fragment: Placing the linker 1.0  $\text{\AA}$  above the equilibrium

position is sufficient to increase the conductance. The origin of this increase will be explained in the next section.

At the Bridge position, a significant rise of the total current is observed as well when the linker molecule is present in the system. Under 1 V bias voltage, the total current of all considered conformations reach the value of about 20  $\mu\text{A}$ , whereas the system without linker reaches  $\sim 18 \mu\text{A}$ . Importantly, by modifying the distance between the linker molecule and the defective ZGNR plane, the total current does not significantly change under the bias voltages investigated here. This observation gives the indication that no drastic quantitative change of the current can be made through varying linker-nanojunction distance at the Bridge absorption site. On the contrary, a more significant current modulation is observed for the variations at the Top position, which is also the energetically more stable conformation.

### 3.4 | Local current density analysis

With the aim of investigating local current properties in the nanojunction, the procedure introduced by Walz et al.<sup>21</sup> combined with two novel numerical improvements described in the Section 2 is applied to selected systems of interest. Various bias voltages are applied for all considered conformations, which are formed by placing the linker molecule either at the Top position or at the Bridge position at various initial distances from the defective ZGNR. All local current densities are represented on a real space grid as described in the Section 2.4. Three different values of bias voltage are selected: 0, 0.5 and 1 V. Note that only the results under 1 V bias voltage are shown here and the local current density maps under 0 and 0.5 V bias voltage are presented in the Figures S8 and S9 for completeness. The side view ( $xz$ -plane) and the top view ( $xy$ -plane) of the local current density maps are integrated along the  $y$ -axis and the  $z$ -axis, respectively.

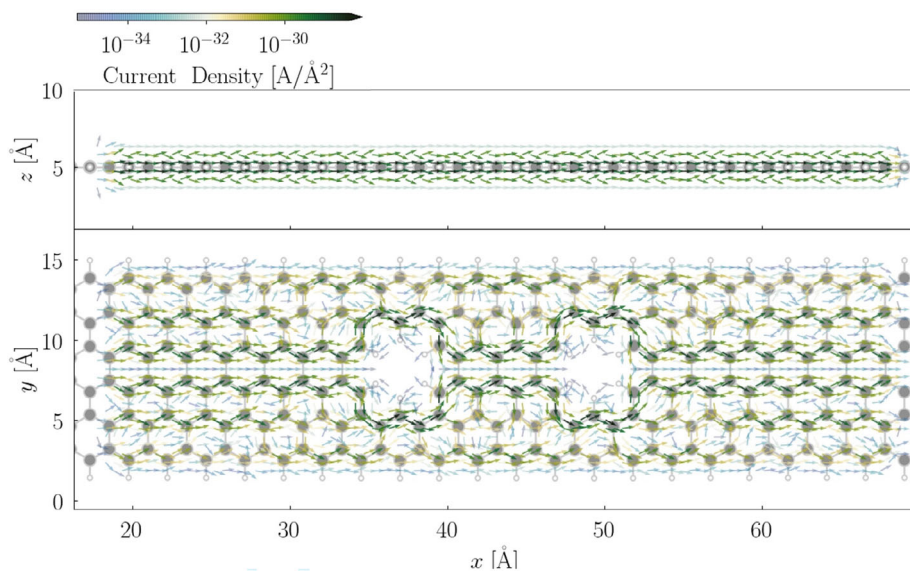


**FIGURE 6** Quiver plot of the electronic current density projected on the real space with 1 units grid spacing of the C–C bonds on the scattering region of no linker system. 1 V bias voltage along the x-axis of the nanojunction plane is applied. For simplification, the flux density is integrated along the y axis of the nanojunction plane for the side view and the flux density is integrated along the z axis of the nanojunction plane for the top view. The intensity of the current density is illustrated according to the color bar, where green indicates the high intensity and blue presents the low intensity

In the system, where no linker molecule is involved, the current density originates from the charge migration only through the  $\pi$ -orbitals. It is shown in Figure 6 from the side (top panel) and the top view (bottom panel). The current flow has a similar appearance as the one shown in Shao et al.<sup>29</sup> for related systems. The electrons flow symmetrically above and below the nanojunction plane and no current density is found perpendicular to that plane. There is a large concentration of the current along the defect edges. The dominant paths for electron transport follow the four central CC lines and they concentrate on the two central ones before spreading when arriving at the defects. As will be shown below, this pattern is found to dominate transport in all systems and conformations considered.

Figures 7 and 8 show a comparison of the current density at different linker heights for the top and bridge adsorption sites. All top views of the local current density have similar attributes, thus, only the current density in the xy-plane for the equilibrium position (at  $Z_{eq}$ ) is shown in the lowest panel of the respective figures. As in the system without linker, the electrons propagate mainly through four middle zigzag paths in defective ZGNRs and the edge of the defects while the ZGNR edge paths are rather unfavorable. Under 0 V bias voltage, the largest magnitude is found to be  $\sim 10^{-38} [\text{A}/\text{\AA}]$ , which explains the vanishingly small conductance for all systems. The local current patterns, shown in the Figure S8, generally flow regularly from the left to right, with some disturbance between the two defects. This irregular stream pattern throughout the system could be an artifact which is below the numerical accuracy and should not be overanalyzed. However, it is still worth mentioning that  $Z_{eq}$ ,  $Z_{eq} - 0.5$ ,  $Z_{eq} - 1.0$  systems at the Top position and  $Z_{eq} - 0.5$  at the Bridge position already show marginal amount of electronic current densities between the linker molecule and the nanojunction surface. This observation demonstrates potential inductive effect of the linker fragment on the defective ZGNRs.

When the applied bias voltage is increased, the small residual current increases and follows the same paths that are already open at

0 V. Under 1 V, the magnitude rises up to  $10^{-30} [\text{A}/\text{\AA}]$ . This is consistent with the increase in total current, see Figure 5. When the linker molecule is placed at the Top position, interference of the local current density between the nanojunction plane and the linker molecule occur. At the equilibrium position (see third panel of Figure 7), the local current density around the leftmost defect shows a marginal increase compared to the bare defective ZGNR, compare top panel of Figure 6. Further, a considerable amount of additional electronic flux can be found in the vicinity of the linker molecule. This would also explain the higher conductance in the system, as shown in the Figure 5. Placing the linker molecule further away from its equilibrium absorption position results in no significant geometric change in the defective ZGNRs plane. This can be observed in both “ $Z_{eq} + 0.5$ ” and “ $Z_{eq} + 1.0$ ” configurations. Consequently, no drastic change of the local current density in the nanojunction is observed.

When the linker is brought closer to the nanojunction plane, stronger influence on the local current pattern around leftmost defect is found. Especially in the lowest configuration, the  $\pi$ -electrons from the linker flow into the  $\pi$ -system of the nanojunction. Two units left of the first defect, a reduction in the local current density is observed in the upper plane of the  $\pi$ -system of the defective ZGNR. This is coupled with an increase in the local current density in lower plane of the  $\pi$ -system. There is also a fair amount of current density in the  $\pi$  system of the pyrene molecule. As the presence of the linker molecule leads to a strong geometric distortion in the defective ZGNRs plane, this has a strong impact on the electrons flow in the  $\pi$  system: The uniformity of the local current density is disturbed and the direction of the electron flux no longer points along the applied bias voltage. Two units right of the linker position in the nanojunction, the regularity of the electron transport pattern is restored, and the current density looks as in the linker-free system. The “ $Z_{eq} - 0.5$ ” configuration exhibits a similar behavior but with less intensity, as the geometric distortion in the nanojunction plane is not very pronounced.

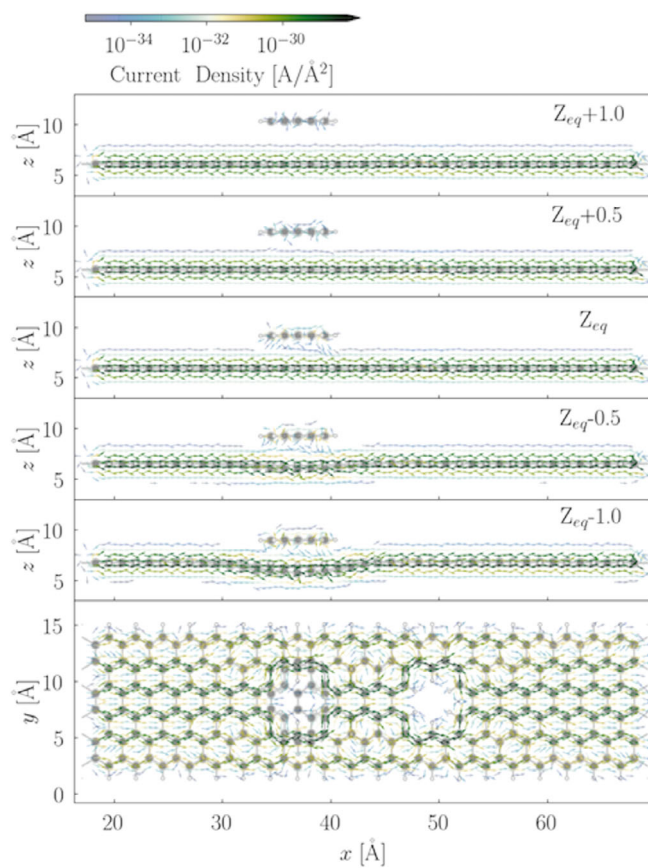


**FIGURE 7** Quiver plot of the electronic current density projected on a real space grid. The local currents on the scattering region are reported for five systems, where the linker molecule is placed at the bridge position with different linker heights with respect to the defective zigzag graphene nanoribbons (ZGNRs). A 1 V bias voltage along the  $x$ -axis of the nanojunction plane is applied. For simplification, the current density is integrated along the  $y$ -axis of the nanojunction plane for the side view. The top view for the  $Z_{eq}$  conformation, integrated along the  $z$ -axis of the nanojunction plane, is shown in the bottom panel. The intensity of the current density is illustrated according to the color bar, where green indicates the high intensity and blue presents the low intensity

At the Bridge position (see Figure 8), the linker molecule also induces an increase in the local current density in the system. However, this effect is less intense in comparison to the conformations with linker on the Top position. For example, when comparing the “ $Z_{eq} - 0.5$ ” conformation for both the Top and the Bridge adsorption sites, a smaller amount of electron flux around the pyrene is observed in the latter position. This demonstrates less interference from the linker to the local current densities of the defective ZGNRs. This is surprising considering the stronger distortion of the ZGNR plane as compared to the adsorption at the Top position. On the other hand, it correlates well to the larger linker-ZGNR distance for the Bridge adsorption. Similar results at both adsorption sites can also be found in most adsorption positions at “ $Z_{eq} + 1.0$ , “ $Z_{eq} + 0.5$ ” and “ $Z_{eq}$ .” In the higher configuration at “ $Z_{eq} + 1.5$ ,” the linker and the ZGNR appear to be decoupled and no extra electron flux is found near the  $\pi$ -system of the linker.

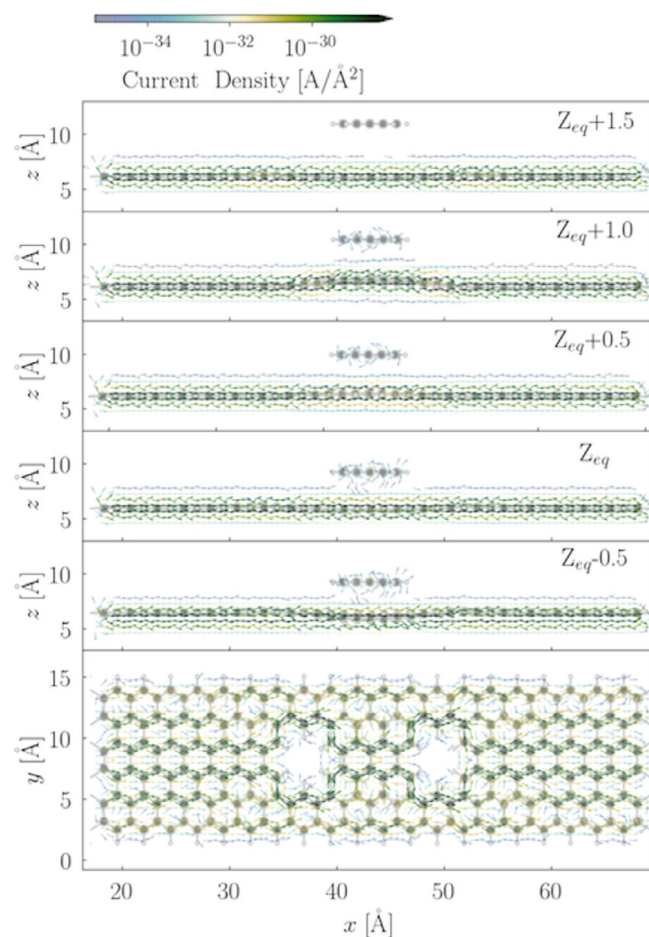


**FIGURE 8** Quiver plot of the electronic current density projected on a real space grid. The local currents on the scattering region are reported for five systems, where the linker molecule is placed at the top position with different linker heights with respect to the defective zigzag graphene nanoribbons (ZGNRs). A 1 V bias voltage along the  $x$ -axis of the nanojunction plane is applied. For simplification, the current density is integrated along the  $y$ -axis of the nanojunction plane for the side view. The top view for the  $Z_{eq}$  conformation, integrated along the  $z$ -axis of the nanojunction plane, is shown in the bottom panel. The intensity of the current density is illustrated according to the color bar, where green indicates the high intensity and blue presents the low intensity

## 4 | DISCUSSION

The interaction between the linker molecule and nanojunction is characterized as a dispersive interaction, which originates from  $\pi-\pi$  interactions.

At the Top adsorption site, due to hexagonal perforations in the defective ZGNRs, there are less interaction possibilities between the linker molecule and this surface region itself. It also means that less repulsion possibly occurs between the two when the linker is brought closer to the ZGNR. This explains not only the lowest absorption energy for this adsorption site, but also the smallest equilibrium distance among examined special points. The presence of the HER2 protein from the experiment is simplified as the distance difference

between the linker molecule and the ZGNR. One common observation is found in both sets of energetic scans (the Top and the Bridge position) described in the previous section: the distance between the linker molecule and the part of the ZGNR just below tends to remain almost at their respective equilibrium distance, even when the initial distance before structure relaxation of the two is modified. Recall that during these structure relaxation runs, the z-position of the linker and of the leads is kept frozen. As a result, the defective ZGNR region beneath the linker molecule experiences detrimental geometrical changes. This can be viewed as a balance between the attraction and the repulsion forces in the system.

The integrated total current-bias voltage dependence shows a clear effect of the linker molecule on the conductance. The projected densities of states (PDOS) on the scattering region is frequently used as a guide or first information on the conduction properties of molecular devices. In the specific cases studied here, this PDOS shows only marginal difference among all considered conformations (see Figure S4), which cannot be easily identified. Hence, these differences provide neither clear qualitative nor quantitative information about its possible relation to the conductance. The transmission function can be viewed as the average transmission probability for electrons to pass through the device along the direction of the applied bias voltage. From the obtained transmission functions (shown in the Figure S3), one can hardly draw clear connections to the change in the conductance nor its geometric origin. Up to 1 V potential bias, only the states between  $\pm 0.5$  V are relevant to explain the transport properties in our system. In the local energy spectrum (see Figures S5 and S6) of the scattering region for the systems we have considered, there is small change near Fermi energy with varying Z-axis of the linker molecule at the Top position, whereas it is not the case for the Bridge position. The variation in the transport properties likely comes from these changes in the coupling with the states in the lead units, where the major contributions are the states near the Fermi energy. As shown in our earlier work, local current density analysis allows one to gain deeper insight of the transport mechanism through the module devices. The local current maps of the considered systems presented above give a clear view of the induced conductive effect from the linker molecule to the defective ZGNRs, as well as of its geometric origin. For the results that linker molecule has stronger larger impact on the conductivity of the defective ZGNRs at its Top position than at its Bridge position, we give two possible reasons. First, since the Top absorption site of the linker molecule blue is found at an equilibrium distance that is 0.2 Å than the Bridge position, stronger  $\pi$ -electron-electron interaction from the linker to the nanojunction surface is expected at closer distances. Second, the linker molecule could be viewed as an extra parallel conductive material which transport some more electrons. In this specific case, the vacancy position is partially refilled when the linker molecule is placed at the Top position, whereas at the Bridge position it is not the case. In the Top positions, it appears that the change in the height is an important structural parameter to explain the repletion of the  $\pi$ -system, left locally depleted by the vacancy. At the Bridge position, the  $\pi$ -system is already rich in electrons and the structure simply adapts to the

strain imposed by the linker in the Z-range investigated here. This result supports the experimental observation, where the GALs surface exhibits higher sensitivity in the conductance with higher protein binding amount in comparison to the pure graphene surface.

Finally, the IV curve result from the additional calculation (see Figure S7) when the linker is 8 Å away does converge to the No-linker system. The linker being close enough to the nanosheet is able to change the total conductivity of the system, even if from the local current density map no electron flux is found near the  $\pi$ -system.

## 5 | CONCLUSION

In this work, systems containing defective ZGNRs and a pyrene molecule as linker have been studied to elucidate their potential biosensing mechanism. Using a dispersion adapted functional, a relatively strong physisorption of the linker molecule on defective ZGNRs is revealed. Due to the reduced repulsion with the surface, the position on top of the defects is found to be the favorable absorption site for the linker molecule. The currents through the device were analyzed in the quasi-static regime using the NEGF formalism. Simply by placing the linker molecule on top of the ZGNR appears to be sufficient to increase the total conductance of the system. This assumption is verified by two sets of total transport calculations for different conformations, where the linker molecule is located either on Top of a given defect or at the Bridge position between defects. Modifying the distance between the linker molecule and the ZGNR simulates the presence of a heavy protein. At the top position, modifying the distance between the linker and the defective ZGNRs is found to allow changing the conductance of the system quantitatively. These results could offer some glimpse of the electron transport mechanism in graphene-based biosensor materials. Binding heavy bio molecules potentially changes the distance between the linker molecule and the defective ZGNR. From a transport perspective, the energetically more stable Top absorption site appears more sensitive to the small quantitative changes of the conductance when varying the height of the linker above the ZGNR plane. It is thus likely to be responsible for the biosensing properties observed in experiment.<sup>11</sup>

To reveal the electron transport mechanism under bias voltage, two novel numerical techniques were introduced to accelerate the computation of local current maps using NEGF—a spectral contraction using the singular value decomposition and spatial filtering via CRS. These developments largely reduce the computational cost associated with the local current analysis procedure, thus providing an efficient tool to gain detailed information about the current patterns through such devices, especially when the quantitative change in the global transport properties is small. In the specific case studied here, we learn that the  $\pi$ -electrons of the linker molecule interact with  $\pi$ -system of the nanojunction, and that this effect is more pronounced when the linker adsorbs on top of a defect. The hypothesis is that there is less repulsion at the linker-ZGNR interface and that the  $\pi$ -electrons of the linker replenish the ZGNR  $\pi$ -system in the defect region. Local current analysis suggests that the  $\pi$ - $\pi$  interaction is responsible for the changes of the conductance in the system and linker

polarization could have an important quantitative effect on the measured current through such devices. Chemical binding to certain biomolecules might lead to a change in the polarization of the linker molecule. This would consequently impact the  $\pi$ - $\pi$  interaction between the linker molecule and the graphene material surface, which is another important factor potentially responsible for the biosensing properties.

## ACKNOWLEDGMENTS

We acknowledge the computer facilities of the Freie Universität Berlin (ZEDAT) for computer time. The authors thank Kangli Wang for fruitful discussions on absorption energies as well as on the graphical representations.

Open access funding enabled and organized by Projekt DEAL.

## DATA AVAILABILITY STATEMENT

Data available on request from the authors.

## ORCID

Jingjing Shao  <https://orcid.org/0000-0003-0980-1093>  
 Beate Paulus  <https://orcid.org/0000-0002-9834-4949>  
 Jean Christophe Tremblay  <https://orcid.org/0000-0001-8021-7063>

## REFERENCES

- [1] K. S. Novoselov, A. K. Geim, S. V. Morozov, D. Jiang, Y. Zhang, S. V. Dubonos, I. V. Grigorieva, A. A. Firsov, *Science* **2004**, *306*, 666.
- [2] A. K. Geim, K. S. Novoselov, *Nanoscience and Technology: A Collection of Reviews from Nature Journals*, World Scientific, London **2010**, p. 11.
- [3] A. K. Geim, *Science* **2009**, *324*, 1530.
- [4] A. H. Castro Neto, F. Guinea, N. M. R. Peres, K. S. Novoselov, A. K. Geim, *Rev. Mod. Phys* **2009**, *81*, 109.
- [5] L. Wang, B. Wu, J. Chen, H. Liu, P. Hu, Y. Liu, *Adv. Mater* **2014**, *26*, 1559.
- [6] L. Liao, X. Duan, *Mater. Sci. Eng. R Rep.* **2010**, *70*, 354.
- [7] S.-K. Lee, H. Y. Jang, S. Jang, E. Choi, B. H. Hong, J. Lee, S. Park, J.-H. Ahn, *Nano Lett* **2012**, *12*, 3472.
- [8] M. Bieri, M. Treier, J. Cai, K. Alt-Mansour, P. Ruffieux, O. Gröning, P. Gröning, M. Kastler, R. Rieger, X. Feng, K. Müllen, R. Fasel, *ChemComm* **2009**, *45*, 6919.
- [9] D.-e. Jiang, V. R. Cooper, S. Dai, *Nano Lett* **2009**, *9*, 4019.
- [10] S. Blankenburg, M. Bieri, R. Fasel, K. Müllen, C. A. Pignedoli, D. Passerone, *Small* **2010**, *6*, 2266.
- [11] Y. Yang, X. Yang, X. Zou, S. Wu, D. Wan, A. Cao, L. Liao, Q. Yuan, X. Duan, *Adv. Funct. Mater* **2017**, *27*, 1604096.
- [12] T. G. Pedersen, C. Flindt, J. Pedersen, N. A. Mortensen, A.-P. Jauho, K. Pedersen, *Phys. Rev. Lett* **2008**, *100*, 136804.
- [13] R. Petersen, T. G. Pedersen, *Phys. Rev. B* **2009**, *80*, 113404.
- [14] J. A. Fürst, J. G. Pedersen, C. Flindt, N. A. Mortensen, M. Brandbyge, T. G. Pedersen, A.-P. Jauho, *New J. Phys* **2009**, *11*, 095020.
- [15] F. Ouyang, S. Peng, Z. Liu, Z. Liu, *ACS Nano* **2011**, *5*, 4023.
- [16] S. Yuan, R. Roldán, A.-P. Jauho, M. I. Katsnelson, *Phys. Rev. B* **2013**, *87*, 085430.
- [17] Z. Liu, Z. Zhao, Y. Wang, S. Dou, D. Yan, D. Liu, Z. Xia, S. Wang, *Adv. Mater* **2017**, *29*, 1606207.
- [18] F. Banhart, J. Kotakoski, A. V. Krasheninnikov, *ACS Nano* **2011**, *5*, 26.
- [19] M. Walz, J. Wilhelm, F. Evers, *Phys. Rev. Lett* **2014**, *113*, 136602.
- [20] J. Wilhelm, M. Walz, F. Evers, *Phys. Rev. B* **2015**, *92*, 014405.
- [21] M. Walz, A. Bagrets, F. Evers, *J. Chem. Theory Comput.* **2015**, *11*, 5161.
- [22] D. Rai, O. Hod, A. Nitzan, *J. Phys. Chem. Lett* **2011**, *2*, 2118.
- [23] D. Rai, O. Hod, A. Nitzan, *J. Phys. Chem. C* **2010**, *114*, 20583.
- [24] G. C. Solomon, C. Herrmann, T. Hansen, V. Mujica, M. A. Ratner, *Nat. Chem* **2010**, *2*, 223.
- [25] T. Ono, Y. Fujimoto, S. Tsukamoto, *Quantum Matter* **2012**, *1*, 4.
- [26] Z. Yu, S. Chen, G. Chen, *Phys. Rev. B* **2013**, *87*, 85110-1-6.
- [27] D. Nozaki, W. G. Schmidt, *J. Comput. Chem* **2017**, *38*, 1685.
- [28] M. Thoss, F. Evers, *J. Chem. Phys* **2018**, *148*, 030901.
- [29] J. Shao, V. Pohl, L. E. M. Steinkasserer, B. Paulus, J. C. Tremblay, *J. Phys. Chem. C* **2020**, *124*, 23479.
- [30] I. Oz, O. Hod, A. Nitzan, *Mol. Phys* **2019**, *117*, 2083.
- [31] V. Pohl, L. E. M. Steinkasserer, J. C. Tremblay, *J. Phys. Chem. Lett* **2019**, *10*, 5387.
- [32] R. S. Mulliken, *J. Chem. Phys* **1955**, *23*, 1833.
- [33] A. Buluç, J. T. Fineman, M. Frigo, J. R. Gilbert, C. E. Leiserson, in *Proc. of the 21st Annu. Symp. on Parallelism in algorithms and architectures 2009*, Association for Computing Machinery New York, NY pp. 233–244.
- [34] J. J. Mortensen, L. B. Hansen, K. W. Jacobsen, *Phys. Rev. B* **2005**, *71*, 035109.
- [35] J. E. Enkovaara, C. Rostgaard, J. J. Mortensen, J. Chen, M. Dulak, L. Ferrighi, J. Gavmolt, C. Glinsvad, V. Haikola, H. A. Hansen, H. H. Kristoffersen, M. Kuisma, A. H. Larsen, L. Lehtovaara, M. Ljungberg, O. Lopez-Acevedo, P. G. Moses, J. Ojanen, T. Olsen, V. Petzold, N. A. Romero, J. Stausholm-Møller, M. Strange, G. A. Tritsaris, M. Vanin, M. Walter, B. Hammer, H. Häkkinen, G. K. H. Madsen, R. M. Nieminen, J. K. Nørskov, T. T. Puska, M. Rantala, J. Schiøtz, K. S. Thygesen, K. W. Jacobsen, *J. Phys. Condens. Matter* **2010**, *22*, 253202.
- [36] M. A. L. Marques, M. J. T. Oliveira, T. Burnus, *Comput. Phys. Commun.* **2012**, *183*, 2272.
- [37] S. Lehtola, C. Steigemann, M. J. T. Oliveira, M. A. L. Marques, *SoftwareX* **2018**, *7*, 1.
- [38] M. Dion, H. Rydberg, E. Schröder, D. C. Langreth, B. I. Lundqvist, *Phys. Rev. Lett* **2004**, *92*, 246401.
- [39] J. Klimeš, D. R. Bowler, A. Michaelides, *J. Condens. Matter Phys.* **2009**, *22*, 022201.
- [40] A. H. Larsen, M. Vanin, J. J. Mortensen, K. S. Thygesen, K. W. Jacobsen, *Phys. Rev. B* **2009**, *80*, 195112.
- [41] A. H. Larsen, J. J. Mortensen, J. Blomqvist, I. E. Castelli, R. Christensen, M. Dulak, J. Friis, M. N. Groves, B. Hammer, C. Hargus, E. D. Hermes, P. C. Jennings, P. B. Jensen, J. Kermode, J. R. Kitchin, E. L. Kolsbjer, J. Kubal, K. Kaasbjer, S. Lysgaard, J. B. Maronsson, T. Maxson, T. Olsen, L. Pastewka, A. Peterson, C. Rostgaard, J. Schiøtz, O. Schütt, M. Strange, K. S. Thygesen, T. Vegge, L. Vilhelmsen, M. Walter, Z. Zeng, K. W. Jacobsen, *J. Phys. Condens. Matter* **2017**, *29*, 273002.
- [42] K. S. Thygesen, M. V. Bollinger, K. W. Jacobsen, *Phys. Rev. B* **2003**, *67*, 115404.
- [43] K. S. Thygesen, K. W. Jacobsen, *Chem. Phys* **2005**, *319*, 111.
- [44] K. S. Thygesen, K. W. Jacobsen, *Phys. Rev. B* **2005**, *72*, 033401.
- [45] M. Strange, I. S. Kristensen, K. S. Thygesen, K. W. Jacobsen, *J. Chem. Phys.* **2008**, *128*, 114714.
- [46] G. Hermann, V. Pohl, J. C. Tremblay, B. Paulus, H.-C. Hege, A. Schild, *J. Comput. Chem* **2016**, *37*, 1511.
- [47] G. Hermann, V. Pohl, J. C. Tremblay, *J. Comput. Chem* **2017**, *38*, 2378.
- [48] V. Pohl, G. Hermann, J. C. Tremblay, *J. Comput. Chem* **2017**, *38*, 1515.

## SUPPORTING INFORMATION

Additional supporting information may be found online in the Supporting Information section at the end of this article.

**How to cite this article:** J. Shao, B. Paulus, J. C. Tremblay, *J Comput Chem* **2021**, *42*(21), 1475. <https://doi.org/10.1002/jcc.26557>